Improved structural properties in homogeneously doped $Sm_{0.4}Ce_{0.6}O_{2-\delta}$ epitaxial thin films: high doping effect on the electronic bands.

Nan Yang[†], Daniel Knez[‡], Giovanni Vinai[‡], Piero Torelli[‡], Regina Ciancio[‡], Pasquale Orgiani[§], and Carmela Aruta[#,*]

AUTHOR ADDRESS

[†] School of Physical Science and Technology, ShanghaiTech University, 201210 Shanghai, China

[‡] CNR-IOM, TASC National Laboratory, I-34149 Trieste, Italy

[§] CNR-SPIN c/o University of Salerno, I-84084 Fisciano, Italy and CNR-IOM, TASC National Laboratory, I-34149 Trieste, Italy

[#] CNR-SPIN c/o University of Roma Tor Vergata, I-00133 Rome, Italy

[*] E-mail: carmela.aruta@spin.cnr.it.

KEYWORDS epitaxial thin films, doped ceria, x-ray spectroscopy, crystal structure, surface reaction.

ABSTRACT: The study of ionic materials on nanometer scale is of great relevance for efficient miniaturized devices for energy applications. The epitaxial growth of thin films can be a valid route to tune the properties of the materials and thus obtain new degrees of freedom in materials design. High crystal quality $Sm_xCe_{1-x}O_{2-\delta}$ films are here reported at high doping level up to x=0.4, thanks to the good lattice matching with the (110) oriented $NdGaO_3$ substrate. X-ray diffraction and transmission electron microscopy demonstrate the ordered structural quality and absence of Sm segregation at macroscopic and atomic level, respectively. Therefore, in epitaxial thin films the homogeneous doping can be obtained even with high dopant content not always approachable in bulk form, getting even an improvement of the structural properties. In situ spectroscopic measurements by x-ray photoemission and x-ray absorption show the O 2*p* band shift towards the Fermi level which can favor the oxygen exchange and vacancy formation on the surface when the Sm doping is increased to x=0.4. X-ray absorption spectroscopy also confirms the absence of ordered oxygen vacancy clusters and further reveals that the 5*d* e_g and t_{2g} states are well separated by the crystal field in the undistorted local structure even in the case of high doping level x=0.4.

INTRODUCTION

Doped and undoped ceria demonstrates excellent redox properties for energy applications, as for example electrochemical catalysis and sensing devices.[1] The redox behavior is related to the switching between Ce^{4+} and Ce^{3+} oxidation states accompanied by the formation and annihilation of oxygen vacancies. The oxygen storage/release capability is crucial for absorbing oxygen and water molecules during the carbon monoxide oxidation and water-gas shift reaction.[2, 3] Many efforts have been devoted to increase the ceria surface activity. On one side, nanostructure engineering has emerged as a useful strategy to enhance the catalytic activity of pure ceria.[4, 5] On the other side, the doping effect with rare earth (RE) elements in ceria was largely investigated to find the optimal doping, in terms of dopant concentration and ion size, to improve the functional properties of ceria.[6, 7] However, conducting and surface reaction properties are strictly correlated. Indeed, after the adsorption of gas molecules on the surface, the oxygen ion should be able to move thorough the bulk.[8] Defect interaction effects were invoked to explain the worsening of the ion conductivity at higher doping levels and the better catalysis performances.[9, 10] Moreover, the advances in the layer by layer growth of thin films allowed different strategies to be used to modulate the ionic conductivity and the catalyzing properties of doped and undoped ceria, taking advantage from the possibility to modify both strain and doping.[11] The role of strain on the conducting and surface reaction properties is still highly debated. Recently, theoretical calculations in the case of ceria demonstrated that biaxial strain in thin films on mismatched substrates is better than the isostatic strain induced by cation substitutions in reducing the formation energy of the oxygen vacancy.[12] The competition between the bulk-like effect of reducing the compressive strain with the formation of larger Ce^{3+} ions and the strain induced tetragonal distortion in thin films was discussed, as well as defect association was also considered as a possible mechanism for the strain relaxation. In thin films, artificial structures were also used to improve the ion conductivity of doped ceria.[13] In particular, it was demonstrated that in nanoscaffold films of Sm doped ceria and Y_2O_3-stabilized ZrO_2 the ion conductivity can be higher than the corresponding conductivity in plain films up to four orders of magnitude. This finding was attributed to the high crystallinity of the nanoscaffold structures. Therefore, we take advantage of advanced thin films growth method to obtain good enough reproducibility of the surface quality to rule out specific surface area effects, together with the possibility to control the strain effects and the structural quality. We previously reported a study of both the oxygen ion conductivity and surface reactivity of epitaxially grown $Sm_xCe_{1-x}O_{2-\delta}$ (SDC) films with different doping levels up to x=0.4.[14] We observed by Raman spectroscopy the occurring of associated defects, which we considered the cause of the improved oxygen exchange surface reaction in heavily doped samples. Nevertheless, literature papers reported that the solubility limit for RE doped bulk samples can vary greatly with regard both the dopant segregation and structural phase stability.[15 - 17] In case of RE=Sm the typical fluorite structure is stable up to about x=0.2-0.4 for bulk samples.[17,18] In case of RE=Gd the solubility limit without dopant segregation is x<0.25.[19] Similarly to other oxide

systems, further excess of RE dopant would favor the formation of spurious phases, mainly RE_2O_3.[20] On the contrary, we report here that SDC thin films grown on (110) oriented $NdGaO_3$ (NGO) substrate with different Sm content up to x=0.4 have a very good crystal structure without structural relaxation associated to the Ce^{3+}/Ce^{4+} formation or Sm segregation. Macroscopic and local structural characterizations by X-ray Diffraction (XRD) and Transmission Electron Microscopy (TEM) measurements, respectively, demonstrate that Sm can homogeneously substitute the Ce in the lattice site of the CeO_2 fluorite structure, with even an improvement of the structural properties in case of the highest doping level we investigated (x=0.4). It is clear that the substrate plays a crucial role in stabilizing the CeO_2-type structure.

We use here a spectroscopic approach to study the implications of this structural improvement on the microscopic properties of the SDC films. Spectroscopic measurements by X-ray photoemission (XPS) and X-ray absorption (XAS) demonstrate that Sm substitution in CeO_2 may induce higher hybridization between O 2*p* and Sm 4*f* electronic bands when x=0.4 due to the O 2*p* band shift.[21] Here, we assume that, similarly to perovskite oxides, the greater availability of O 2*p* states close to the Fermi level lowers the energy needed to exchange oxygen ions on the surface of epitaxial SDC fluorite thin films.[22] We therefore demonstrate that epitaxial growth of thin films can be effectively used to explore larger spectrum of material composition, which allows to obtain new nanoscale materials for miniaturized electrochemical devices.

METHODS

Thin film deposition. SDC thin films with different Sm content (x = 0, 0.1, 0.2, 0.4) are grown by pulsed laser deposition (PLD) on NGO substrate with thickness about 30 nm. A KrF excimer pulsed laser source with a typical energy density of about 2 J/cm^2 and a laser repetition rate of 5 Hz was used. SDC targets were made through solid reactions between CeO_2 (99.9% purity) and Sm_2O_3 (99.99% purity) powders and synthesized at 1200°C for 12 hours. The growth temperature was set to 600°C under an oxygen background pressures of 1×10^{-2} mbar. Such a value has been proven to induce a very small amount of oxygen vacancies. As a matter of fact, undoped CeO_2 thin films show bulk-like lattice parameters with no sign of reduction of the out-of-plane lattice parameter (see Supporting Information), which has been proved to be associated to oxygen vacancies in CeO_2 materials.[15]

X-ray Diffraction. XRD measurements were performed with a Philips X'Pert-XRD analytic diffractometer equipped with a four-circle cradle using a Cu Kα source, which allowed reciprocal space maps and azimuthal scans of the asymmetrical reflections.

Transmission Electron Microscopy. Cross-sectional TEM analysis and selected area electron diffraction (SAED) were performed using a JEOL 2010 UHR TEM operated at 200 kV and equipped with a field emission gun. The scanning TEM (STEM) attachment coupled with energy-disperse x-ray spectrometer was used to obtain chemical profiles. TEM samples were prepared by conventional polishing followed by dimpling and milling with Ar ions.

Spectroscopic measurements by synchrotron radiation. XPS and XAS techniques were used to measure samples grown in-situ by the PLD system directly connected to the transfer chamber of APE-HE beamline at Elettra synchrotron in Trieste. The *in-situ* transferring procedure limits the surface contaminants effects and guarantees that the samples are all measured under identical conditions, so that a reliable comparison of surface properties *vs.* doping concentration can be performed. XPS measurements were recorded with an Omicron EA125 hemispherical electron energy analyzer, with the sample at 45° with respect to the impinging linearly polarized light and normal to the surface. XAS measurements were taken in total electron yield (TEY) mode, at room temperature, normalizing the intensity of the sample current to the incident photon flux current at each energy value, in horizontal polarization, with an incident angle of 45°.

RESULTS AND DISCUSSION

The bulk structure of undoped CeO_2 is cubic fluorite type with lattice parameters a = 5.4116 Å.[15] When CeO_2 is grown on NGO, having an orthorhombic structure with a=5.426 Å, b=5.496 Å and c= 7.707 Å, the in-plane lattice cell results rotated 45°, as demonstrated by the XRD azimuthal scan reported in Supporting Information. The NGO[002]//SDC[110] in plane epitaxial relationship between NGO and CeO_2 is particularly favorable because the mismatch, calculated as $m = (a_{sub} - a)/a_{sub}$ where a_{sub} is the in-plane diagonal of NGO and a is the bulk value of SDC, is very low, being about 0.8% in pure CeO_2. In addition, the in-plane mismatch is further reduced when increasing the doping with Sm down to about 0.1% for SDC40. XRD θ-2θ scan shows the only presence of (00l) reflections (see Supporting Information) demonstrating the single phase and orientation of the samples. The *c*-axis parameters are reported in Figure 1(a). Their experimental determination has been obtained by fitting the (002) peak position by a gaussian line shape and considering the 90-to-100% criteria. We can observe the *c*-axis elongation with increasing the Sm content, from 5.41 Å (CeO_2, x=0) to 5.44 Å (SDC, x=0.4), in agreement with our previous results.[14] The elongation with x seems in agreement with Vegard's law, because of the substitution of Ce^{4+} with the larger Sm^{3+} cation. Nevertheless, the comparison with the SDC bulk behavior, also reported in Figure 1(a), shows that the *c*-axis elongation is lower than expected, with the largest discrepancy for SDC40. In case of thin films grown on mismatched substrate, as in our SDC films grown on NGO, the in-plane lattice is forced to grow along a particular lattice direction to minimize the strain field determined by the above-mentioned epitaxial relationship with the substrate. The XRD reciprocal space maps of Figure 1(c) confirm it and show that SDC films are fully in-plane matched with the NGO substrate. However, the in-plane tensile strain should lead to the *c*-axis contraction accordingly to the elasticity theory, namely *c*-axis decreases when *a*-axis increases. On the contrary, we can see that the undoped ceria *c*-axis corresponds to the bulk value (Figure 1(a)), demonstrating that the mismatch is too low to induce an elastic contraction of the *c*- axis. In addition, the in-plane mismatch is lower for higher doping level, thus the effect of the elasticity theory on the *c*-axis variation becomes even more negligible with increasing the Sm content. However, the effect of charge compensated defects on the *c*-axis variation, such as oxygen vacancy V_o, defect association and Ce^{3+} formation, can also be considered. In fact, oxygen vacancy V_o and defect association may induce lattice contraction and larger Ce^{3+} ions may induce lattice expansion.[15, 18, 23]

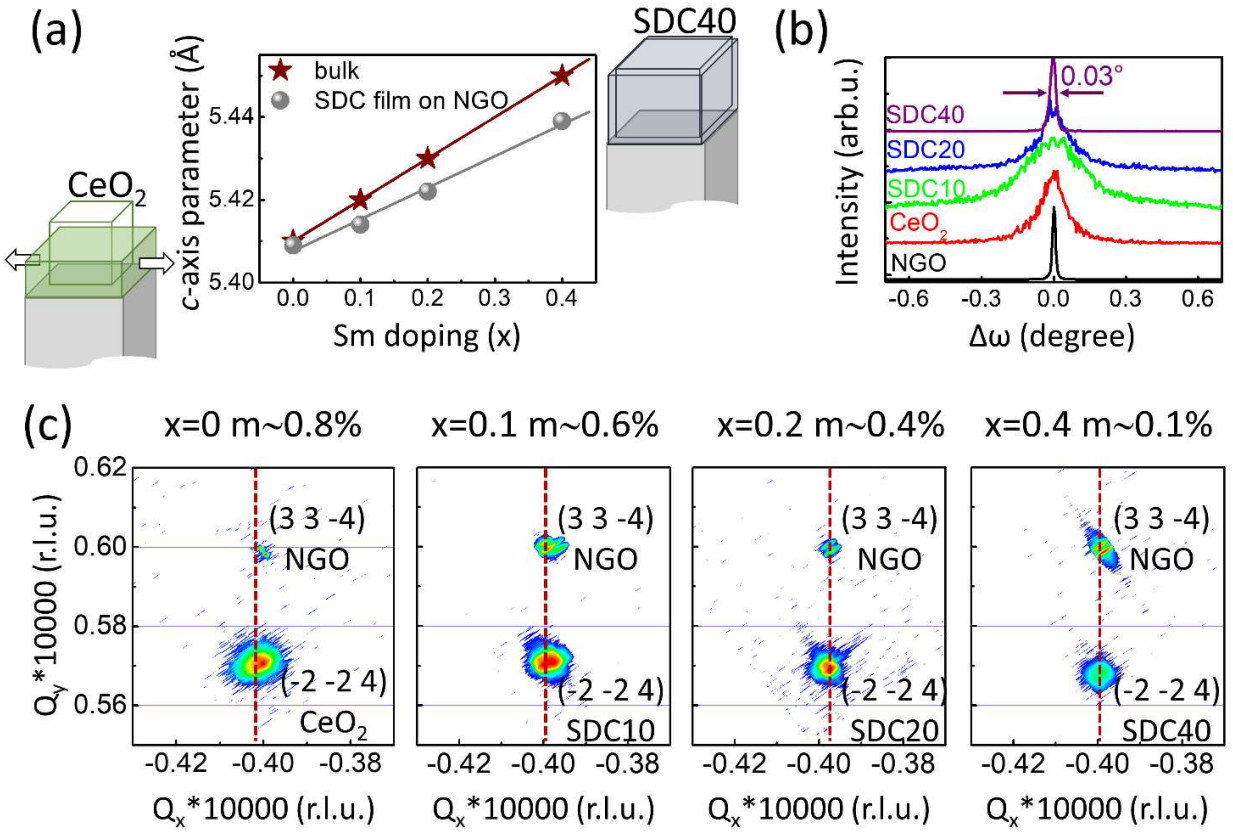

Figure 1. XRD measurements on $Sm_xCe_{1-x}O_{2-\delta}$ (SDC) thin films with x = 0, 0.1, 0.2, 0.4. (a) *c*-axis behavior obtained from the (002) Bragg reflection in symmetrical configuration, compared with that of SDC bulk behaviour. On the bottom-left, sketch of the smallest undoped CeO_2 crystallographic cell undergoing tensile strain when grown on NGO susbtrate. On the up-right, sketch of the largest SDC40 crystallographic cell, almost unstrained when grown on NGO substrate. (b) Rocking curve across the (002) Bragg reflection in symmetrical configuration. (c) Asymmetrical reciprocal space maps around the (33-4) Bragg reflection of NGO substrate and (-2-24) Bragg reflection of SDC films.

In addition, shorter cation−cation distances than expected from the ion packing effect were also pointed out for SDC granular samples.[23] It was reported that the anion sublattice expands while the cation sublattice contracts.[23] We cannot discriminate here among the different contributions of the above mentioned lattice contraction factors in determining the largest discrepancy between film and bulk *c*-axis in the case of x=0.4 Sm doping level. Nevertheless, we can surely conclude from the XRD data that the template made by the substrate allows the growth of good quality SDC films, especially with the highest doping concentrations. In fact, all the samples have a very narrow rocking curve, as shown in Figure 1(b), in particular SDC40 has the narrowest rocking curve, comparable with that of the substrate thanks to the lowest mismatch between film and substrate. It is worth to remark that in polycrystalline doped CeO_2 bulk samples high doping levels may results in RE dopant segregation.[18, 25] Such a scenario can be sustained by XRD investigation on those samples, which is expected to show no variation in the SDC XRD peaks positions, i.e. saturation in structural and/or chemical composition of doped CeO_2 and, more important, the appearing of Sm_2O_3 diffraction peaks. On the contrary, XRD investigation of our SDC films shows no sign of diffraction peaks assessable to any spurious phase for all Sm doping levels.

Further details on the film nanostructure were provided by High Resolution TEM analysis. A representative bright field HRTEM image of the film/substrate cross sectional region is shown in Figure 2. The film is about 33 nm-thick, has a high crystalline quality and a very good alignment with the bare substrate. This is further enlightened by the corresponding fast Fourier transform (FFT) shown in Figure 2(b) that confirms the expected epitaxial [110]//[002] relationship between film and substrate and the good matching of the relative in-plane direction. The FFTs are obtained from film (yellow) and substrate (cyan) regions separately and are combined in one image for direct comparison. Closer details on the film nanostructure are provided by selected area electron diffraction pattern (SAED) performed on the film only. In the SAED pattern of Figure 2(c) no signs of additional phases or structural disorder are seen, thus confirming, under the experimental uncertainty, the absence of crystalline regions due to Sm segregation inside the film.[19, 25] These results are in full agreement with XRD data. We would like to point out that the influence of the Sm content on local oxygen ordering is not directly visible in SAED, due to the low scattering contribution of the oxygen sublattice compared to the

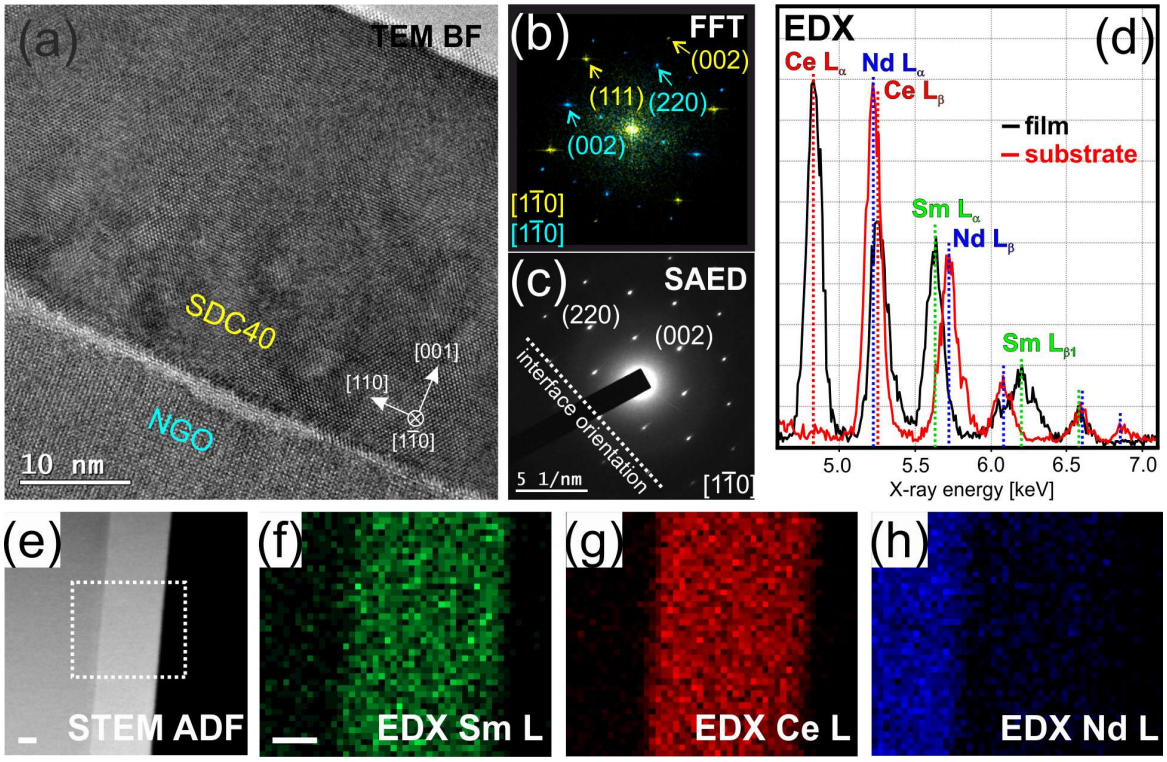

Figure 2. HRTEM analysis of the Sm doped film with x=0.4 (SDC40): (a) HRTEM bright field (BF) micrograph showing substrate and film. (b) FFT from the film (yellow) and substrate region (cyan). (c) SAED pattern of the film. (d) EDX analysis comparing the film and the substrate. (e) STEM ADF image showing film on the substrate, the green rectangle marks the region chosen for EDX elemental mapping. (f-h) EDX elemental maps for Sm, Ce and Nd, respectively. Scale bars in (e-h) are 10 nm.

heavier atoms in the crystal. Insights on the chemical assessment of the film and, especially, on the Sm chemical distribution were obtained by Energy Dispersive X-ray Analysis (EDX) and Z- contrast imaging. The plot in Figure 2(d) shows EDX spectra acquired from the film and the substrate, focusing on the energy region of the Sm L peak family. The expected peaks of the elements of the film and of the substrate are clearly discernable, though exact elemental quantification is hindered by significant peak overlapping. STEM annular dark field coupled with EDX elemental maps was used to ascertain the spatial distribution of Sm within the film. It is important to remark that Annular Dark Field (ADF) detector is very sensitive to the atomic number Z, therefore allowing to appreciate the presence of local chemical variations inside the film by Z-contrast imaging.[19] Figure 2(e) shows a STEM ADF image of the film (brighter contrast) and substrate (darker contrast). The film region exhibits a homogeneous contrast with no presence of brighter contrast regions that would account for Sm clustering (i.e. lower density regions). EDX elemental maps for Sm L, Nd L and Ce L peaks acquired on the spatial region highlighted by the dashed rectangle in Figure 2(e) are displayed respectively in Figure 2(f), (g) and (h). In all the maps, the substrate/films interface appears straight and continuous, indicating negligible sample drift during data acquisition. The Sm signal is homogeneously distributed inside the film region thus ruling out the presence of Sm clustering inside the film. It is important to point out that the Sm signals measured in the substrate region must be considered as a background resulting from the overlapping Sm L, Nd L and Ce L peak families, which cannot be subtracted from the EDX data.

Besides structural ones, the Sm doping in CeO_2 also has important effects on the density of states (DOS). Therefore, the Sm cation itself may affect the surface reactions by changing the electronic states available on the surface for the bonding with the adsorbates. In Figure 3(a) the valence band (VB) spectra, i.e. the DOS close to the Fermi level, for undoped CeO_2 and SDC films with x=0-0.4, are reported. The very apparent feature at about 2 eV from the Fermi level in the CeO_2 spectra corresponds to the electronic configuration of Ce^{3+} ($4f^1$), which implies the presence of one extra electron into the 4*f* localized band. We can observe a shift of the VB edge with Sm doping in agreement with the theoretical TDOS calculations by Dong-Hee Lim *et al.*, which demonstrate that the O 2*p* band shifts with increasing the Sm doping.[21] The magnification close to the Fermi level region is reported in Figure 3(b) for the CeO_2 and SDC40 films, where the Sm 4*f* hybridized with O 2*p* and Ce $4f^1$

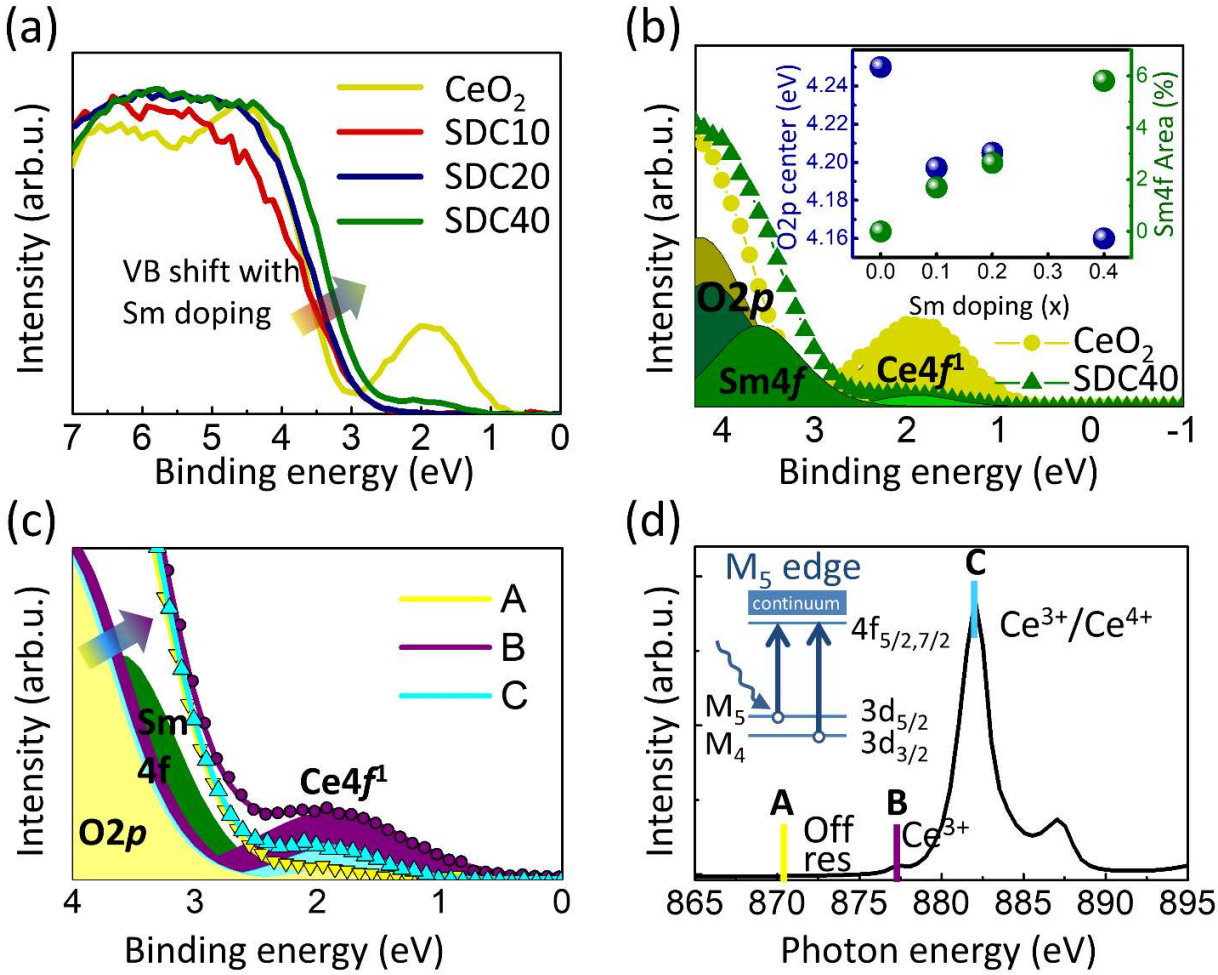

Figure 3. (a) VB spectra *in-situ* measured with 495 eV photon excitation energy for undoped CeO_2 and SDC with x=0-0.4 in the energy range 0-7 eV. (b) Magnification of panel (a) of undoped CeO_2 and SDC40 films in the range 0-4.3 eV. The colored dashed regions point out the different contributions to the VB obtained by fitting after subtracted a Shirley background. The O 2*p* band center energy and Sm 4*f* area obtained from the fit are reported in the inset. (c) VB resonant photoemission close to the Fermi level of the SDC40 film measured at different photon excitation energies labelled with A-C corresponding to the photon energy of Ce 3*d* XAS spectrum reported in panel (d).

fit components are highlighted (see Supporting Information for further details on the fit procedure). The O 2*p* binding energy (BE) and Sm 4*f* relative area obtained from the fit are reported in the inset for the different samples. It can be observed that the Sm 4*f* band area increases and the O 2*p* band shifts towards the Fermi level with increasing the Sm content. The Sm 4*f* band area behavior is in agreement with the nominal Sm concentration of our films. The O 2*p* band shift is an interesting finding since it may explain the better oxygen reactivity on the surface, as theoretically demonstrated in the case of desulfurization process.[21] Such a correlation between the improved surface reactivity and the higher hybridization between O 2*p* and metal orbitals was largely reported in the case of perovskites.[22, 26, 27] We guess here that similar effects may have an important role in the case of the fluorite structure, namely the O 2*p* shift decreases the formation energy of oxygen vacancies and improves the surface reactivity. In the VB spectra the contribution from the $4f^1$ can be observed not only in undoped ceria, but also in heavily doped Sm doped ceria SDC40. The presence of $4f^1$ in the SDC40 film is confirmed by resonant photoemission VB spectra (Figure 3(c)) measured in resonance at the absorption edge of Ceria from 3*d* to 4*f* levels shown in Figure 3(d).[28] The O 2*p*-Sm 4*f* hybridized band and Ce $4f^1$ fit components are also shown. The enhancement of the feature associated to the single electron $4f^1$ is evident when the absorption is in resonance with the energy of pure Ce^{3+} (absorption energy labelled as B). This finding confirms the enhancement of the Ce^{3+} content when ceria is heavily doped at x=0.4. We can also observe that the VB leading edge moves towards the Fermi level when the photon energy is at resonance with the energy of pure Ce^{3+}. Assuming that the Sm 4*f* band does not change with changing the absorption photon energy, the fit was performed changing the O 2*p* band energy eventually hybridized with Ce 5*d* 4*f*.[29] This finding demonstrates that the O 2*p* band shifts closer to the Fermi level

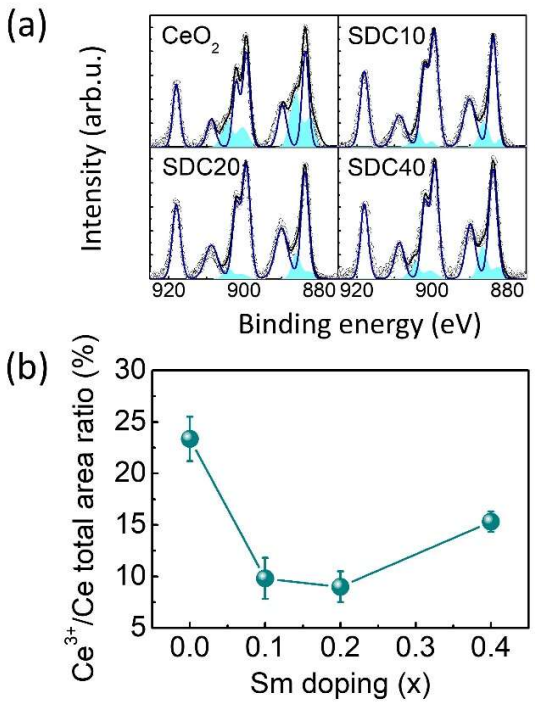

Figure 4. (a) Ce 3*d* XPS spectra measured with 1260 eV photon excitation energy of undoped CeO_2 and doped SDC films with x=0-0.4. Spectra are normalized to unity after subtraction of the Shirley background. (b) Area ratio of Ce^{3+} peaks and the total spectrum area *vs.* the Sm doping.

in resonance at the Ce^{3+} energy, indicating the O 2*p* shift is strictly related to the Ce^{3+} formation.

The behavior of the Ce^{3+} content with changing the amount of doping is obtained by XPS measuring the Ce 3*d* core level spectra. The results for SDC films with x=0-0.4 are reported in the Figure 4 (a). Ce 3*d* photoemission peak presents a rich multiple structure in which are present both Ce^{4+} and Ce^{3+} contributions, each of them with $3d_{5/2}$ and $3d_{3/2}$ spin-orbit splitting peaks and other splittings related to the core hole effect on the energy level redistribution. However, the Ce^{4+} and Ce^{3+} contributions can be clearly identified by fitting procedure.[7] Further details are reported in Supporting Information. The sum of all Ce^{4+} peaks is drawn by the blue solid line, while the sum of all Ce^{3+} peak areas is highlighted by the cyan filled area. The relative amount of Ce^{3+} can be calculated from the relative peak areas.[30] In Figure 4(b) we can observe that the Ce^{3+} concentration decreases with Sm-doping from about 23% for the pure CeO_2 to about 10% for the SDC films with x=0.1-0.2 and then increases again to about 15% for x=0.4 getting the largest Ce^{3+} concentration for the doped samples. Since the films are well oxidized during the growth and they have been transferred *in-situ* from the PLD chamber to the XPS one, the high Ce^{3+} values may be affected by the ultra-high vacuum environment during the XPS measurements (pressure 1 x 10^{-10} mbar). In fact, the films may lose oxygen from the surface due to the high vacuum conditions and the Ce^{3+} absolute values may not be reliable. However, since all the samples are measured in the same conditions, the behavior of Figure 3(b) is trustworthy and gives an indication of the intrinsic different stability of the Ce^{4+}/Ce^{3+} redox couple with different Sm content. When increasing the Sm doping up to x=0.1-0.2, the decreasing of the Ce^{3+} content can be a consequence of the charge imbalance compensation by Sm^{3+} ions instead of Ce^{3+}.[31] Further increasing the Sm doping, an unexpected increase of Ce^{3+} is observed. It has been reported that oxygen exchange reaction with Ce^{3+} formation can be favored by the association of defects.[10, 32] Our previous Raman spectroscopy measurements have already shown the uprising of an associated defect band at doping concentrations heavier than 20% mol Sm, where higher surface reactivity was also found. However, the evolution of the surface chemistry induced by Sm doping was not included.[14] We subsequently reported that Ce^{3+} concentration in doped ceria epitaxial films may depend on the dopant ionic radius.[7] In agreement with theoretical calculations, it was suggested that cations with smaller ionic radius allow the releasing of the stress strength accumulated when the larger Ce^{3+} is formed in the lattice site of the smaller Ce^{4+} ion.[7, 33] Since Sm ion has a higher radius size than Ce one, we can rule out the local structural relaxation effects. Therefore, we assume that the driving force for the unexpected Ce^{3+} increase for SDC x=0.4 is the formation of defect association between Ce^{3+} and V_o, as for example dimer $[Ce'_{Ce}V_O^{\bullet\bullet}]^{\bullet}$ and trimer $[Ce'_{Ce}V_O^{\bullet\bullet}Ce'_{Ce}]^{x}$ previously identified by Raman spectroscopy, which can be obtained by the reactions reported in Supporting Information.[14]

The electronic structure close to the Fermi level was further investigated by XAS at the O K-edge, which gives information on the metal-ligand (Ce-O and Sm-O) hybridizations.[34] In Figure 5(a) the evolution of the O K-edge spectra with different doping content is reported. Three main features can be distinguished, named A, B and C, which are respectively assigned to the hybridized O 2*p* states with Ce^{4+} 4*f* (feature A at about 530eV) and with e_g and t_{2g} (B at about 532.5 eV and C at about 537 eV) of Ce^{4+} 5*d* states.[35] O K-edge XAS spectra of Ce^{3+} and Sm^{3+} have less sharp features and are few eV shifted at higher photon energy.[36] Therefore, the increased Ce^{3+} and Sm^{3+} content can be macroscopically visualized from the increased intensity in the valleys between the Ce^{4+} 5*d* features (see arrows in Figure 5(a)) labelled as B' and C'. The intensity of A peak changes upon doping with Sm, reaching the minimum for the SDC40 film. The 4*f* orbital filling due to the change in the electronic configuration from Ce^{4+} ($4f^0$) to Ce^{3+} ($4f^1$) and the increased amount of Sm^{3+} ($4f^5$) implies a change in the hybridization of the O 2*p*–Ce/Sm 4*f* states, and therefore the variation of A peak intensity reflects the 4*f* occupancy.[37] The decreased intensity of Ce 4*f* peak for high Sm doping levels suggests a reduction of the unoccupied 4*f* states, which indicates an increase of 4*f* occupied states according to the increase in Ce^{3+} and Sm^{3+} concentration. Another interesting information that can be obtained from the XAS spectra concerns the crystal field effects. In an ideal fluorite structure, Ce/Sm ions are in the center of a cube cage and bounded by eight oxygen ions in the corner of the cube. The consequent crystal field of the cubic symmetric eightfold coordination reflects on the B and C peaks, which corresponds to 5*d* t_{2g} and e_g hybridized with O 2*p* orbitals. Therefore, the energy separation of the B and C peaks ΔE(C-B)

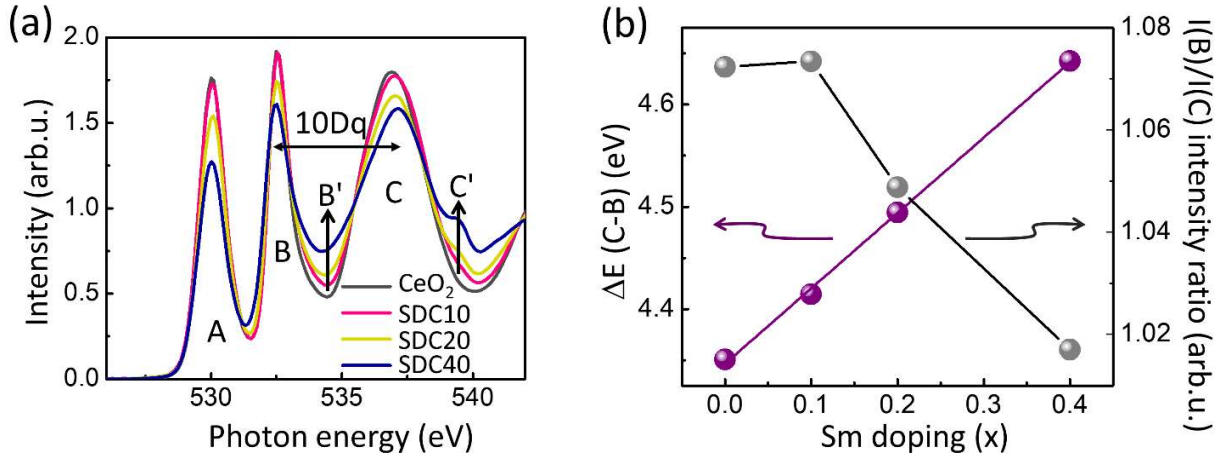

Figure 5. (a) XAS at O K-edge of CeO_2 undoped and doped with different Sm doping epitaxial films. (b) Energy separation between the C and B peaks ΔE(C-B) together with the intensity relative ratio of the same peaks as a function of the Sm doping. The linear fit of the ΔE(C-B) data is also reported.

reflects the *d*-orbitals splitting between t_{2g} and e_g. Owing to the different orientation of t_{2g}*(dxy, dxz, dyz)* and e_g*(dx²-y², dz²)* orbitals, the Ce/Sm 5*d* t_{2g} should be more hybridized with O 2*p* orbitals. Therefore, the t_{2g}-derived oxygen peak (here labelled as C) should be stronger in the ideal case of Ce^{4+} only in undoped stoichiometric CeO_2. However, the presence of Ce^{3+} and Sm^{3+} ions may result in mixing of the e_g and t_{2g} states, widening the peaks and changing their relative intensity and energy separation. In particular, it has been reported that oxygen vacancies ordering/disordering cause an increase/decrease in peak B intensity.[38] The I(B)/I(C) intensity ratio reported in Figure 5(b) shows a decreasing behavior, despite very small, as a function of the Sm x stoichiometry, which might indicate the absence of ordered oxygen vacancy clusters when increasing the doping content. In addition, we can observe that the energy separation ΔE(C-B) reported in Figure 5(b) linearly increases with Sm content x. This demonstrates the stronger crystal field effect in case of higher Sm doping. The increased crystal field indicates that the e_g and t_{2g} states are well separated by the cubic symmetrical eightfold coordination when increasing the doping with Sm, as a consequence of an undistorted local structure. In an ideal case of well separated atomic levels, two factors could further contribute in changing the crystal field strength, namely the charges and the distances of the ligands from oxygen. The linear behavior of ΔE(C-B) is in disagreement with the effect of the charges since Ce^{3+} concentration behavior is not linear (see Figure 4b). It is also in disagreement with the effect of bond distances, since the O-Sm bond length are longer, in accordance to the linear increasing of the c-axis reported in Figure 1(a) and previous Raman measurements.[14] Therefore, differently from the bulk and pellets cases, when highly doped ceria films have a very good matching with the substrate, a very well ordered crystal structure can be obtained with homogeneous distribution of oxygen vacancies, without defect cluster formation, as we demonstrate here in the case of x=0.4 Sm ceria films grown on NGO substrate.[38-41]

CONCLUSION

The epitaxial growth of thin films can be a valid route to tune the properties of the materials. We show that high crystal quality SDC thin films with different Sm content x=0-0.4 can be epitaxially grown on (110) oriented NGO substrate. The *c*-axis parameter linearly increases up to the highest doping level investigated (x=0.4) as expected for the homogeneous substitution of the larger Sm ion into the Ce lattice site of the fluorite structure. However, the largest discrepancy between the bulk and film lattice values in the case of SDC with x=0.4 can be ascribed to contraction factors such as oxygen vacancies or defect associations. XRD measurements show the absence of spurious phases and the perfect lattice matching between film and substrate, as well as a very small rocking curve, which is greatly reduced just in the SDC40 film, namely in the case of the largest Sm content. Transmission electron microscopy (TEM) confirms the homogenous distribution of Sm dopant cation in the high quality fluorite structure.

XPS and XAS measurements allow us to explain on the basis of electronic structure analysis the lowering of the activation energy of the oxygen exchange reaction followed by Ce^{3+} formation. XPS data show that Ce^{3+} concentration has a non linear behavior, which first decreases with Sm up to x=0.2 and then increases for x=0.4. Higher hybridization between O 2*p* and Sm 4*f* electronic bands is observed in the VB measurements both on- and off-resonance, which is mainly a consequence of the O 2*p* band shift. This finding, together with the improved $Ce^{4+} \rightarrow Ce^{3+}$ reduction properties, can be an indication of lower formation energy of oxygen vacancies when the Sm content is increased up to x=0.4. XAS results also show that the 5*d* e_g and t_{2g} states are well separated by the crystal field in the undistorted local structure even in case of SDC films with higher Sm content, in agreement with the structural quality observed by XRD and TEM.

While in the field of nanoelectronics – which deals with the electronic carriers – the epitaxial growth is widely employed to tune the properties of the materials, we demonstrate here that the same approach can be efficiently adopted also in the so-called field of nanoionics, namely the study of ion conducting materials on nanometer scale. Indeed, the proper choice of the substrate to be used as a template in the film growth may allow

to obtain material compositions that cannot be otherwise obtained in the bulk form, together with an improvement of the structural properties with respect to the undoped samples. The approach of tailoring and combining the properties of ion conducting materials using thin films can be of great relevance in the field of energy research for efficient miniaturized devices.

ASSOCIATED CONTENT

Supporting Information. The Supporting Information is available free of charge via the Internet at http://pubs.acs.org.

Further X-ray diffraction (S1); X-ray Photoemission Spectroscopy analysis (S2); further details on the X-ray absorption at the O K-edge (S3); main chemical reactions involved in $Sm_xCe_{1-x}O_{2-\delta}$ film (S4).

AUTHOR INFORMATION

Corresponding Author

* Carmela Aruta - CNR-SPIN c/o University of Roma Tor Vergata, I-00133 Rome, Italy;

E-mail: carmela.aruta@spin.cnr.it.

ACKNOWLEDGMENT

This work has been partly performed in the framework of the Nanoscience Foundry and Fine Analysis (NFFA-MIUR Italy Progetti Internazionali) facility in Trieste, Italy. The authors thank E. Cociancich for TEM specimen preparation.

REFERENCES

(1) Montini, T; Melchionna, M.; Monai, M.; Fornasiero, P. Fundamentals and Catalytic Applications of CeO_2-based Materials. *Chem. Rev*. **2016**, 116, 5987−6041.

(2) Avakyan, L. A.; Kolpacheva, N. A.; Paramonova, E. V.; Singh, J.; Hartfelder, U.; van Bokhoven, J. A.; Bugaev, L. A. Evolution of the Atomic Structure of Ceria-Supported Platinum Nanocatalysts: Formation of Single Layer Platinum Oxide and Pt−O−Ce and Pt−Ce Linkages. *J. Phys. Chem. C* **2016**, 120, 28057−28066.

(3) Trovarelli, A. Catalytic Properties of Ceria and CeO_2-containing Materials. *Catal. Rev.: Sci. Eng.* **1996**, 38,439−520.

(4) Zhou, K.; Wang, X.; Sun, X.; Peng, Q.; Li, Y. Enhanced Catalytic Activity of Ceria Nanorods from Well-Defined Reactive Crystal Planes. *J. Catal.* **2005**, 229, 206−212.

(5) Sun, C.; Sun, J.; Xiao, G.; Zhang, H.; Qiu, X.; Li, H.; Chen, L. Mesoscale Organization of Nearly Monodisperse Flowerlike Ceria Microspheres. *J. Phys. Chem. B* **2006**, 110, 13445−13452.

(6) Kilner, J.A. Fast Oxygen Transport in Acceptor Doped Oxides. *Solid State Ionics* **2000**, 129, 13–23.

(7) Yang, N.; Orgiani, P.; Di Bartolomeo, E.; Foglietti, V.; Torelli, P.; Ievlev ,A. V.; Rossi, G.; Licoccia, S.; Balestrino, G.; Kalinin, S. V.; Aruta, C. Effects of Dopant Ionic Radius on Cerium Reduction in Epitaxial Cerium Oxide Thin Films. *J. Phys. Chem. C* **2017**, 121, 8841-8849.

(8) Feng, Z. A.; El Gabaly, F.; Ye, X.; Shen, Z.-X.; Chueh, W. C. Fast Vacancy-mediated Oxygen Ion Incorporation Across the Ceria – Gas Electrochemical Interface. *Nat. Commun.* **2014**, 5, 4374.

(9) Grieshammer, S.; Grope, B. O. H.; Koettgen, J.; Martin, M. A Combined DFT + U and Monte Carlo Study on Rare Earth Doped Ceria. *Phys. Chem. Chem. Phys.* **2014**, 16, 9974−9986.

(10) Esch, F.; Fabris, S.; Zhou, L.; Montini, T.; Africh, C.; Fornasiero, P.; Comelli, G.; Rosei, R. Electron Localization Determines Defect Formation on Ceria Substrates. *Science* **2005**, 309, 752−755.

(11) Aidhy, D. S.; Weber, W. J. Microstructure Design for Fast Oxygen Conduction. *J. Mater. Res.* **2016**, 31, 2-16.

(12) Gopal, C. B.; García-Melchor, M.; Lee, S. C.; Shi, Y.; Shavorskiy, A.; Monti, M.; Guan, Z.; Sinclair, R.; Bluhm, H.; Vojvodic, A.; Chueh, W. C. Equilibrium Oxygen Storage Capacity of Ultrathin $CeO_{2-\delta}$ Depends Non-monotonically on Large Biaxial Strain. *Nat. Commun.* **2017**, 8, 15360.

(13) Yang, S. M.; Lee, S.; Jian, J.; Zhang, W.; Lu, P.; Jia, Q.; Wang, H.; Noh, T. W.; Kalinin S. V.; MacManus-Driscoll, J. L. Strongly Enhanced Oxygen Ion Transport Through Samarium-doped CeO_2 nanopillars in Nanocomposite Films. *Nat. Commun.* **2015**, 6, 8588.

(14) Yang, N.; Shi, Y.; Schweiger, S.; Strelcov, E.; Belianinov, A.; Foglietti, V.; Orgiani, P.; Balestrino, G.; Kalinin, S. V.; Rupp, J. L. M.; Aruta, C. Role of Associated Defects in Oxygen Ion Conduction and Surface Exchange Reaction for Epitaxial Samaria-Doped Ceria Thin Films as Catalytic Coatings. *ACS Appl. Mater. Interfaces* **2016**, 8, 14613−14621.

(15) Artini, C.; Pani, M.; Carnasciali, M.; Plaisier, J. R.; Costa, G. A. Lu^-, Sm^-, and Gd-Doped Ceria: A Comparative Approach to Their Structural Properties. *Inorg. Chem.* **2016**, 55, 10567−10579.

(16) Coduri, M.; Checchia, S.; Longhi, M.; Ceresoli, D.; Scavini, M. Rare Earth Doped Ceria: the Complex Connection Between Structure and Properties. *Front. Chem.* **2018**, 6, 526.

(17) Artini, C.; Massardo, S.; Carnasciali, M. M.; Joseph, B.; Pani, M. In Situ High Pressure Structural Investigation of Sm-Doped Ceria. *Energies* **2020**, 13, 1558.

(18) Zhang, J.; Ke, C.; Wu, H.; Yu, J.; Wang, J.; Wang, Y. Solubility Limits, Crystal Structure and Lattice Thermal Expansion of Ln_2O_3 (Ln=Sm, Eu, Gd) doped CeO_2. *J. Alloys Compd.* **2017**, 718, 85-91.

(19) Li, Z.-P.; Mori, T.; Auchterlonie, G. J.; Zou, J.; Drennan, J. Direct Evidence of Dopant Segregation in Gd-Doped Ceria. *Appl. Phys. Lett.* **2011**, 98, 093104.

(20) Joy, P. A.; Sankar, C. R.; Date, S. K. The Limiting Value of x in the Ferromagnetic Compositions $La_{1-x}MnO_3$. *J. Phys.: Condens. Matter* **2002**,14, L663.

(21) Lim, D.-H.; Kim, H. S.; Yoon, S. P.; Han, J.; Yoon, C. W.; Choi, S. H.; Nam S. W.; Ham, H. C. Mechanisms of Enhanced Sulfur Tolerance on Samarium (Sm)-Doped Cerium Oxide (CeO_2) from First Principles. *Phys. Chem. Chem. Phys.* **2014**, 16, 10727.

(22) Hwang, J.; Rao, R. R.; Giordano, L.; Katayama, Y.; Yu, Y.; Shao-Horn, Y. Perovskites in Catalysis and Electrocatalysis. *Science* **2017**, 358,751-756.

(23) Nakamura, A. New Defect-Crystal-Chemical Approach to Non-Vegardianity and Complex Defect Structure of Fluorite-Based MO_2–$LnO_{1.5}$ Solid Solutions (M^{4+}=Ce, Th; Ln^{3+}=lanthanide) Part I: Model Description and Lattice-Parameter Data Analysis. *Solid State Ionics* **2010**, 181, 1543−1564.

(24) Giannici, F.; Gregori, G.; Aliotta, C.; Longo, A.; Maier, J.; Martorana, A. Structure and Oxide Ion Conductivity: Local Order, Defect Interactions and Grain Boundary Effects in Acceptor-Doped Ceria. *Chem. Mater.* **2014**, 26, 5994−6006.

(25) Li, Z.-P.; Mori, T.; Ye, F.; Ou, D.; Zou, J.; Drennan, J. Ordered Structures of Defect Clusters in Gadolinium-Doped Ceria. *J. Chem. Phys.* **2011**, 134, 224708.

(26) Zhu, Z.; Shi, Y.; Aruta, C.; Yang, N. Improving Electronic Conductivity and Oxygen Reduction Activity in Sr-Doped Lanthanum Cobaltite Thin Films: Cobalt Valence State and Electronic Band Structure Effects. *ACS Appl. Energy Mater.* **2018**, 1, 5308−5317.

(27) Shi, Y.; Xie, R.; Liu, X.; Zhang, N.; Aruta, C.; Yang, N. Tunable pH-Dependent Oxygen Evolution Activity of Strontium Cobaltite Thin Films for Electrochemical Water Splitting. *Phys. Chem. Chem. Phys.* **2019**, 21, 16230-16239.

(28) Matolín, V.; Matolínová, I.; Sedláček, L.; Prince, K. C.; Skála, T. A Resonant Photoemission Applied to Cerium Oxide Based Nanocrystals. *Nanotechnology* **2009**, 20, 215706.

(29) Chen, H.-T.; Choi, Y. M.; Liu, M.; Lin, M. C. A Theoretical Study of Surface Reduction Mechanisms of CeO_2 (111) and (110) by H_2. *ChemPhysChem* **2007**, 8, 849 – 855.

(30) Borchert, H.; Frolova, Y. V.; Kaichev, V. V.; Prosvirin, I. P.; Alikina, G. M.; Lukashevich, A. I.; Zaikovskii, V. I.; Moroz, E. M.; Trukhan, S. N.; Ivanov, V. P.; Paukshtis, E. A.; Bukhtiyarov, V. I.; Sadykov, V. A. Electronic and Chemical Properties of Nanostructured Cerium Dioxide Doped with Praseodymium. *J. Phys. Chem. B* **2005**, 109, 5728.

(31) Yang, N.; Belianinov, A.; Strelcov, E.; Tebano, A.; Foglietti, V.; Di Castro, D.; Schlueter, C.; Lee, T.-L.; Baddorf, A. P.; Balke, N.; Jesse, S.; Kalinin, S. V.; Balestrino, G.; Aruta, C. Effect of Doping on Surface Reactivity and Conduction Mechanism in Samarium-Doped Ceria Thin Films. *ACS Nano* **2014**, 8, 12494-12501.

(32) Chueh, W. C.; McDaniel, A. H.; Grass, M. E.; Hao, Y.; Jabeen, N.; Liu, Z.; Haile, S. M.; McCarty, K. F.; Bluhm, H.; El Gabaly, F. Highly Enhanced Concentration and Stability of Reactive Ce^{3+} on Doped CeO_2 Surface Revealed In Operando. *Chem. Mater.* **2012**, 24, 1876−1882.

(33) Marrocchelli, D.; Bishop, S. R.; Tuller, H. L.; Yildiz, B.Understanding Chemical Expansion in Non-Stoichiometric Oxides: Ceria and Zirconia Case Studies. *Adv. Funct. Mater.* **2012**, 22, 1958-1965.

(34) Bianconi, A.; Marcelli, A.; Dexpert, H.; Karnatak, R.; Kotani, A.; Jo, T.; Petiau, J. Specific Intermediate-Valence State of Insulating 4f Compounds Detected by L_3 X-ray Absorption. *Phys. Rev. B* **1987**, 35, 806.

(35) Mullins, D. R.; Overbury, S. H.; Huntley, D. R. Electron Spectroscopy of Single Crystal and Polycrystalline Cerium Oxide Surfaces. *Surf. Sci.* **1998**, 409, 307–319.

(36) Altman, A. B.; Pacold, J. I.; Wang, J.; Lukens W. W.; Minasian, S. G. Evidence for 5d-σ and 5d-π Covalency in Lanthanide Sesquioxides from Oxygen K-edge X-ray Absorption Spectroscopy. *Dalton Trans.* **2016**, 45, 9948.

(37) Rodriguez, J. A.; Hanson, J. C.; Kim, J.-Y.; Liu, G.; Iglesias-Juez, A.; Fernández-García, M. Properties of CeO_2 and $Ce_{1-x}Zr_xO_2$ Nanoparticles: X-ray Absorption Near-Edge Spectroscopy, Density Functional, and Time-Resolved X-ray Diffraction Studies. *J. Phys. Chem. B* **2003**, 107, 3535-3543.

(38) Ou, D. R.; Mori, T.; Ye, F.; Zou, J.; Auchterlonie, G.; Drennan, J. Oxygen-Vacancy Ordering in Lanthanide-Doped Ceria: Dopant-Type Dependence and Structure Model. *Phys. Rev. B* **2008**, 77, 024108.

(39) Li, Z.-P.; Mori, T.; Ye, F.; Ou, D.; Auchterlonie, G. J.; Zou, J.; Drennan, J. Cerium-Reduction-Induced Defects Clustering, Ordering, and Associated Microstructure Evolution in Yttrium-Doped Ceria. *J. Phys. Chem. C* **2012**, 116, 5435−5443.

(40) Ou, D. R.; Mori, T.; Ye, F.; Kobayashi, T.; Zou, J.; Auchterlonie, G.; Drennan, J. Oxygen Vacancy Ordering in Heavily Rare-Earth-Doped Ceria. *Appl. Phys. Lett.* **2006**, 89, 171911.

(41) D'Angelo, A. M.; Liu, A. C. Y.; Chaffee, A. L. Oxygen Uptake of Tb−CeO_2: Analysis of Ce^{3+} and Oxygen Vacancies. *J. Phys. Chem. C* **2016**, 120, 14382−14389.

For Table of Contents Only